

Soft Matter

Accepted Manuscript



This is an *Accepted Manuscript*, which has been through the Royal Society of Chemistry peer review process and has been accepted for publication.

Accepted Manuscripts are published online shortly after acceptance, before technical editing, formatting and proof reading. Using this free service, authors can make their results available to the community, in citable form, before we publish the edited article. We will replace this *Accepted Manuscript* with the edited and formatted *Advance Article* as soon as it is available.

You can find more information about *Accepted Manuscripts* in the [Information for Authors](#).

Please note that technical editing may introduce minor changes to the text and/or graphics, which may alter content. The journal's standard [Terms & Conditions](#) and the [Ethical guidelines](#) still apply. In no event shall the Royal Society of Chemistry be held responsible for any errors or omissions in this *Accepted Manuscript* or any consequences arising from the use of any information it contains.

Homeotropic nano-particle assembly on degenerate planar nematic interfaces: films and droplets

Alejandro Londoño-Hurtado,¹ Julio C. Armas-Pérez,¹ Juan P. Hernández-Ortiz,^{2,1,*} and Juan J. de Pablo^{1,†}

¹*Institute for Molecular Engineering, University of Chicago, Chicago, IL*

²*Departamento de Materiales y Minerales, Universidad Nacional de Colombia, Sede Medellín, Colombia*

(Dated: May 12, 2015)

A continuum theory is used to study the effects of homeotropic nano-particles on degenerate planar liquid crystal interfaces. Particle self-assembly mechanisms are obtained from careful examination of particle configurations on a planar film and on a spherical droplet. The free energy functional that describes the system is minimized according to Ginzburg-Landau and stochastic relaxations. The interplay between elastic and surface distortions and the desire to minimize defect volumes (boojums and half-saturn rings) is shown to be responsible for the formation of intriguing ordered structures. As a general trend, the particles prefer to localize at defects to minimize the overall free energy. However, multiple metastable configurations corresponding to local minima can be easily observed due to the high energy barriers that separate distinct particle arrangements. We also show that by controlling anchoring strength and temperature one can direct liquid-crystal mediated nanoparticle self-assembly along well defined pathways.

Keywords: Liquid Crystals, Landau-de Gennes, Ginzburg-Landau relaxation, monte-carlo, nanoscale assembly

I. INTRODUCTION

Liquid Crystals (LC) represent highly tunable media whose morphology can be tailored for specific applications. Parameters, such as confinement, surface anchoring, temperature as well as the chemistry of the material, can all be manipulated to create desirable morphologies [1–6]. The versatility of LCs can be further augmented through addition of nanoparticles. Indeed, intricate couplings between particle anchoring and LC structure can lead to unusual phase transformations that do not arise in simple, unstructured fluids [4, 7–10]. Such couplings can in turn be used for a wide range of applications, including sensing [3, 11].

Colloidal particles in liquid crystals are known to self-assemble into ordered structures. The precise nature of such structures depends on the orientation or anchoring of the liquid crystal at the particle's interface. Two homeotropic nano-particles, for example, may undergo a dipolar interaction, characterized by a hedgehog or point defect, or a quadrupolar interaction, associated a saturn-ring or line defect [12]. Many-particle arrangements can consist of linear chains, periodic lattices or spherical aggregates, to name a few [13–18].

In experiments, anchoring is controlled through chemical treatments, and procedures exist to achieve perpendicular (homeotropic) or parallel (planar) orientations ranging from weak to to strong anchoring. The preferred alignment of the LC at a particle surface may induce distortions in the LC media that result in formation of topological defects that serve to localize particles at specific positions [19, 20]. For example, recent experiments on polystyrene particles at flat LC interfaces show that the

particles can adopt intriguing ordered structures [8]. On curved interfaces, the particles are localized in the boojum defects [21]. Simulations using a many-body model have helped explain the origin of such localization [10].

Note, however, that past computational studies of nanoparticles at curved LC interfaces have been limited to particles that exhibit planar anchoring. Furthermore, such studies were limited to nanoscale droplets with radii in the range of 50 nm. In this work, we present a detailed study of homeotropic particle self-assembly at LC droplet interfaces (see Fig. 1). We adopt a continuum thermodynamic description in terms of Landau-de Gennes free energy functional. In contrast to past studies of nanoparticles suspended in LCs, we adopt a novel Monte Carlo (MC) [22] relaxation method that allows one to arrive at optimal nanoparticle arrangements without the need for educated guesses. Overall, we find that particles exhibit well-defined configurations that are consistent with limited available experimental data [11].

The manuscript is organized as follows: we first describe the thermodynamic model and the relaxation methods employed in our calculations. We then present and discuss our results for one, two and three particles adsorbed on a LC film and on a LC droplet. We conclude with a summary of the main observations and a brief discussion of open questions and future work.

II. THERMODYNAMIC MODEL

The Landau-de Gennes continuum description of the LC employed here relies on the second moment of the director vector, \mathbf{n} , and the second-order alignment tensor, \mathbf{Q} [23, 24], given by:

$$\mathbf{Q}(\mathbf{x}, t) = \mathbf{M}_{\text{II}}(\mathbf{x}, t) - \frac{\delta}{3}, \quad (1)$$

* E-mail: jphernandez@unal.edu.co

† E-mail: depablo@uchicago.edu

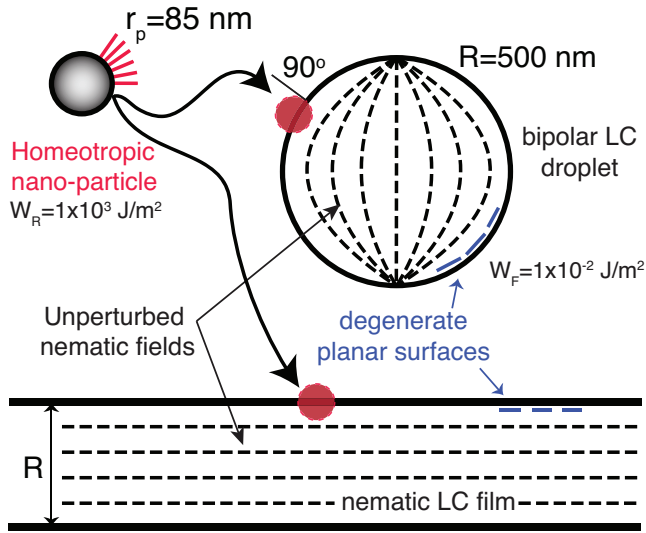


FIG. 1. Schematic representation of the modeled system. Homeotropic nano-particles are embedded in degenerate planar liquid crystalline interfaces with a wetting angle of 90° . The particles perturb the nematic field within the LC. This perturbation is different depending on the curvature of the interface.

where δ is 3×3 is the identity tensor, and the second moment is given by:

$$\mathbf{M}_{\text{II}} = \int \mathbf{n}\mathbf{n}\psi(\mathbf{n}, \mathbf{x}, t) d\mathbf{n}. \quad (2)$$

Here, $\psi(\mathbf{n}, \mathbf{x}, t)$ is the configuration distribution function of molecular orientations. The tensor order parameter can be expressed in terms of its eigenvalues and eigenvectors as follows [25, 26]:

$$\mathbf{Q} = S \left[\mathbf{n}\mathbf{n} - \frac{\delta}{3} \right] + \eta [\mathbf{n}'\mathbf{n}' - (\mathbf{n} \times \mathbf{n}')(\mathbf{n} \times \mathbf{n}')], \quad (3)$$

where $S(\mathbf{x})$ is the scalar order parameter, related to the maximum eigenvalue $2S/3$. The biaxiality $\eta(\mathbf{x})$ is related to the other two eigenvalues $\pm\eta - S/3$. S and η are bounded by: $S \in [-1/2, 1]$ and $\eta \in [-1/3(1-S), +1/3(1-S)]$. The eigenvectors, \mathbf{n} and \mathbf{n}' , corresponding to the maximum and second largest eigenvalues, define an orthonormal basis $\{\mathbf{n}, \mathbf{n}', (\mathbf{n} \times \mathbf{n}')\}$ for the LC orientation. Homogeneous nematic configurations have been found to be uniaxial, and it is commonly assumed that $\eta(\mathbf{x})$ is zero [23–25]. This approximation, however, is not appropriate in the presence of defects [27–29].

Since the alignment tensor is symmetric and traceless, only five out of its nine cartesian components are independent. Here we take advantage of a tensor basis to write \mathbf{Q} in compact form according to [30–32],

$$\mathbf{Q}(\mathbf{x}, t) = \sum_{\nu} a_{\nu}(\mathbf{x}, t) \mathbf{T}^{\nu}, \quad (4)$$

where the orthonormal basis is defined by five tensors:

$$\begin{aligned} \mathbf{T}^1 &= \sqrt{3/2} [\mathbf{z}\mathbf{z}]^{\text{ST}} = \sqrt{3/2} (\delta_{33} - \delta_{ij}/3), \\ \mathbf{T}^2 &= \sqrt{2} [\mathbf{x}\mathbf{y}]^{\text{ST}} = \sqrt{2} (\delta_{1i}\delta_{2j} + \delta_{2i}\delta_{1j})/2, \\ \mathbf{T}^3 &= \sqrt{2} [\mathbf{x}\mathbf{z}]^{\text{ST}} = \sqrt{2} (\delta_{1i}\delta_{3j} + \delta_{3i}\delta_{1j})/2, \\ \mathbf{T}^4 &= \sqrt{1/2} (\mathbf{x}\mathbf{x} - \mathbf{y}\mathbf{y}) = \sqrt{1/2} (\delta_{1i}\delta_{1j} - \delta_{2i}\delta_{2j}), \\ \mathbf{T}^5 &= \sqrt{2} [\mathbf{y}\mathbf{z}]^{\text{ST}} = \sqrt{2} (\delta_{2i}\delta_{3j} + \delta_{3i}\delta_{2j})/2, \end{aligned} \quad (5)$$

where \mathbf{x} , \mathbf{y} and \mathbf{z} are the canonical \mathbb{R}^3 basis, $[\mathbf{A}]^{\text{ST}}$ is a symmetric-traceless projection operation, and δ_{ij} is the Kronecker delta. Because the $\{\mathbf{T}^m\}$ basis is orthonormal,

$$\text{tr}(\mathbf{T}^m \mathbf{T}^n) = T_{ij}^m T_{ij}^n = \delta_{mn}, \quad (6)$$

ensures that the five scalar components a_{ν} of the alignment tensor represent simple projections, i.e.

$$a_{\nu} = \text{tr}(\mathbf{Q}\mathbf{T}^{\nu}). \quad (7)$$

Thus, instead of dealing with nine components and the corresponding constraint equations, we can efficiently specify a configuration of the alignment tensor field, $\mathbf{Q}(\mathbf{x})$, through the set of five independent scalar fields $a_{\nu}(\mathbf{x})$.

The thermodynamic description of the LC is provided by the free energy functional $F(\mathbf{Q})$. It includes a short-range contribution that captures the isotropic-nematic transition, f_L (the Landau energy density), and a long-range elastic contribution that penalizes deformations from a homogeneous state, f_E (the elastic energy density). LC-surface interactions are represented by a surface free energy density, f_S . The resulting free energy functional is thus given by [23, 24, 33]:

$$F(\mathbf{Q}) = \int d^3\mathbf{x} [f_L(\mathbf{Q}) + f_E(\mathbf{Q})] + \oint d^2\mathbf{x} f_S(\mathbf{Q}). \quad (8)$$

The Landau short-range free energy density may be expressed as a polynomial expansion of the tensor invariants [33–35]:

$$f_L = \frac{A}{2} \left(1 - \frac{U}{3} \right) \text{tr}(\mathbf{Q}^2) - \frac{AU}{3} \text{tr}(\mathbf{Q}^3) + \frac{AU}{4} \text{tr}(\mathbf{Q}^2)^2, \quad (9)$$

where A and U are phenomenological coefficients that are functions of temperature (or concentration) and pressure. A sets a scale for the energy density, while U controls the isotropic-nematic transition [13, 24, 36–38].

The elastic energy density is obtained from a model proposed by Oseen, Zocher and Frank [39–43]. In terms of the alignment tensor it is defined by [1, 23]

$$f_E = \frac{1}{2} L_1 \frac{\partial Q_{ij}}{\partial x_k} \frac{\partial Q_{ij}}{\partial x_k}, \quad (10)$$

where

$$L_1 = \frac{1}{6S^2} (k_{33} - k_{11} + 3k_{22}), \quad (11)$$

quantifies the orientational elasticity of the LC. The "k" constants are the elastic moduli that describe the independent modes of deformation: splay (k_{11}), twist (k_{22}) and bend (k_{33}) [25]. In this work, we adopt a single-elastic-constant approximation $k_{11} = k_{22} = k_{33}$ that satisfies the Ericksen inequalities [44] and the stability ranges proposed both by Gartland *et al.* [45] and Longa *et al.* [28].

The surface free energy density describes the interaction of the liquid crystal with a surface. For homeotropic anchoring, we use a Rapini-Papoular [46–50] energy density,

$$f_{S,R} = \frac{1}{2} W_R (\mathbf{Q} - \mathbf{Q}_\perp)^2, \quad (12)$$

where W_R represents the strength of the homeotropic anchoring and \mathbf{Q}_\perp is the perpendicular tensor preferred at the surface, defined as follows:

$$\mathbf{Q}_\perp = S \left[\boldsymbol{\nu}\boldsymbol{\nu} - \frac{1}{3}\boldsymbol{\delta} \right] \quad (13)$$

Here, $\boldsymbol{\nu}(\mathbf{x})$ is the normal unit vector at any point \mathbf{x} along the surface. A degenerate planar anchoring is included through the 4th order Fournier-Galatola energy density [51],

$$f_{S,F} = \frac{1}{2} W_F (\overline{\mathbf{Q}} - \overline{\mathbf{Q}}_\perp)^2 + \frac{1}{4} W_F (\overline{\mathbf{Q}} : \overline{\mathbf{Q}} - S^2)^2, \quad (14)$$

where $\overline{\mathbf{Q}} = \mathbf{Q} + S\boldsymbol{\delta}/3$, $\overline{\mathbf{Q}}_\perp = \mathbf{p} \cdot \overline{\mathbf{Q}} \cdot \mathbf{p}$ is the tensor projection on the surface and $\mathbf{p} = \boldsymbol{\delta} - \boldsymbol{\nu}\boldsymbol{\nu}$.

The physical properties of the LC serve to set three characteristic length scales: the nematic coherence length ξ_N , the homeotropic extrapolation length ξ_R and the planar extrapolation length ξ_F :

$$\xi_N = \sqrt{L_1/A}, \quad \xi_R = L_1/W_S, \quad \xi_{F,1} = L_1/W_F. \quad (15)$$

The nematic coherence length represents the distance over which local fluctuations are correlated, whereas the extrapolation length defines the relative strength between the bulk elasticity to the surface anchoring. The nematic coherence length sets a scale for the free energy functional, $A\xi_N^3 = L_1\xi_N$, and relaxation time, $\gamma\xi_N^2/L_1$, where γ is the LC rotational viscosity coefficient.

III. FREE ENERGY FUNCTIONAL MINIMIZATION

Depending on the length scales of interest, LC systems can be described in terms of continuum approaches [52–57], coarse-grained many-particle models with molecular dynamics (MD) or Monte Carlo (MC) simulations [7, 9, 58–60] or simpler but faster lattice Monte Carlo simulations [61–64]. Continuum techniques rely on a minimization of the free energy functional in order to find the equilibrium state of the LC. Conventional

minimization techniques, however, can get trapped in metastable states. An alternative to conventional energy minimization was proposed by Gruhn and Hess [65]. In their work, the authors used an MC algorithm to find the equilibrium director field for a Lebwohl-Lasher model. Ruhwandl and Terenjev [66] proposed a related MC algorithm to solve a simplified form of the free energy functional [66] around a spherical inclusion in a uniform nematic LC matrix. In this work, we build on their ideas by performing free energy minimizations using a Ginzburg-Landau (GL) and Monte Carlo (MC) relaxations, but we do so by relying on the orthonormal representation introduced earlier (in terms of the $a_\nu(\mathbf{x})$ scalars), thereby ensuring a uniform, unbiased sampling of configuration space.

For the simple GL relaxation, using a \mathbf{Q} description, a projector operator $\Pi_{\mathbf{Q}}$, is defined according to the natural construction of the tensor \mathbf{Q} : symmetric and traceless,

$$\Pi_{\mathbf{Q}}(\mathbf{B}) = \frac{1}{2} (\mathbf{B} + \mathbf{B}^T) - \frac{1}{3} \text{tr}(\mathbf{B}) \boldsymbol{\delta}, \quad (16)$$

for any $\mathbf{B}(\mathbf{x}) \in \mathbb{R}^3 \times \mathbb{R}^3$ with $\mathbf{x} \in V$ and $\mathbf{x} \in \sigma_S$ (domain and boundary). The free energy must satisfy the following Euler-Lagrange equations:

$$\Pi_{\mathbf{Q}} \left(\frac{\delta F}{\delta \mathbf{Q}} \right) = 0, \quad (17)$$

for $\mathbf{x} \in V$ and

$$\Pi_{\mathbf{Q}} \left(\frac{\delta F}{\delta \nabla \mathbf{Q}} \cdot \boldsymbol{\nu} \right) = 0, \quad (18)$$

as boundary conditions ($\mathbf{x} \in \sigma_S$). The Volterra derivatives are defined by [67]:

$$\frac{\delta F}{\delta \mathbf{Q}} = \frac{\partial F}{\partial \mathbf{Q}} - \frac{\partial}{\partial \mathbf{x}} \cdot \frac{\partial F}{\partial \nabla \mathbf{Q}}. \quad (19)$$

The solutions to these equations are found by allowing the tensor order parameter \mathbf{Q} to evolve towards equilibrium according to a GL relaxation equation of the form

$$\frac{\partial \mathbf{Q}}{\partial t} = -\frac{1}{\gamma} \left[\Pi_{\mathbf{Q}} \left(\frac{\delta F}{\delta \mathbf{Q}} \right) \right], \quad (20)$$

with boundary conditions given in Eqn. (18) and where γ is a rotational viscosity (or diffusion) coefficient [48, 68, 69].

MC relaxations, using the $\{\mathbf{a}\}$ representation, start with the random selection of a domain or surface point \mathbf{x}_k . The tensor is changed, by a random amount, according to

$$Q_{ij}(\mathbf{x}_k) \rightarrow Q_{ij}(\mathbf{x}_k) + \xi_{ij}, \quad (21)$$

where ξ_{ij} are cartesian components of a random, symmetric and traceless tensor. This is achieved by adding a uniform deviate ξ_i (in some prescribed interval $[\xi_{\min}, \xi_{\max}]$)

to one of the scalar fields: $a_\nu(\mathbf{x}_k) \rightarrow a_\nu(\mathbf{x}_k) + \xi_\nu$. Following the standard Metropolis algorithm, a trial change to the alignment tensor field is accepted with probability

$$P_{\text{acc}} = \min(1, \exp[-\beta\Delta F]). \quad (22)$$

If the update is accepted, we simply record the new value of the total free energy and begin a new iteration; if the update is rejected, we restore the alignment tensor to its previous value and continue with a new iteration. The Metropolis parameter β can be interpreted in terms of the spatial scale of the system, and is useful for developing advanced Monte Carlo algorithms, such as simulated annealing or parallel tempering that combine simulations with different values of β . For simplicity, in this work we implemented an annealing scheme that starts from a low value of β and steadily increases to facilitate sampling early on and identify stable states at later stages.

Spatial derivatives and free energy functionals were approximated by a Finite Difference Method (FDM) using second order approximations for both the GL and MC relaxations. A fully explicit first order Euler method was employed for time integration in the GL relaxation. Characteristic length and time scales, prescribed by the nematic coherence length, are resolved numerically during the approximation. The FDM scheme was composed by 1'426,880 nodes and the time step was equivalent to 0.01 times the characteristic nematic relaxation time $\gamma\xi_N^2/L_1$. For the GL relaxation, total computational times were equivalent to 20,000 to 50,000 characteristic times, with a final tolerance for the free energy difference of 1×10^{-10} . For MC relaxations, the inverse temperature was decreased exponentially from 1×10^{-2} to 1×10^{-12} during the entire relaxation. A typical MC simulation needed around 1'000,000 MC moves with a 30% acceptance criteria.

IV. RESULTS

Simulations were performed using 4'-penty-4-cyanobiphenyl (5CB) liquid crystal [33, 70]: $A \approx 1 \times 10^5$ J/m³ and $k_{11} \approx 5 - 7 \times 10^{-12}$ N, resulting in a nematic coherence length $\xi_N = 7.15$ nm. The parameter U , in the Landau free energy density, was determined from

$$S_{\text{bulk}} = \frac{1}{4} + \frac{3}{4} \sqrt{1 - \frac{8}{3U}}. \quad (23)$$

For a bulk system in the isotropic phase, this parameter is expected to have values of $U < 8/3$ ($S_{\text{bulk}}=0.41$). For a system in the nematic phase, $U \geq 5.0$ ($S_{\text{bulk}}=0.76$) [37, 71]. In this work, we used values of $U = 3.0$ and $U = 5.0$ ($S_{\text{bulk}} = 0.5$ and $S_{\text{bulk}} = 0.76$) as the initial order parameter.

We considered nano-particles with radius $r_p = 85$ nm, modeled as spheres that are half-submerged in the LC films or droplets. The anchoring at these particles is homeotropic with infinite strength. We studied a planar

film (infinite curvature) of thickness $R = 500$ nm, and a droplet of radius $R = 500$ nm. The LC anchoring at these interfaces is planar degenerative. The anchoring strength on the LC interfaces is $W_F = 1 \times 10^{-2}$ J/m².

We start by examining a planar interface with one, two and three particles. The particle distribution is fixed and several initial conditions are studied to explore the free energy landscape. Relaxations by GL and MC can be pursued simultaneously, and final configurations can be exchanged to guarantee that a global minimum is indeed identified.

A. Planar LC film

Figure 2 shows the director field (\mathbf{n}) for a system that was initially oriented along the x -axis (the $(1, 0, 0)$ direction). The figure presents side views for one, two and three particles, together with the director field and the defects around the particles, which consist of half-Saturn rings. For the director field, the blue color indicates an orientation along the preferred direction of the bulk, while red corresponds to a perpendicular orientation. The strong homeotropic anchoring on the particles clashes with the director field in the film, leading to gradients that result in defects. These distortions reach a maximum in the regions where the LC director and the particle are normal. For the systems considered here, the defects induced by the particles, remain localized next to the particles, i.e. there is only a short-range relaxation of the LC away from the particles.

Addition of nanoparticles to a droplet induces deformations that increase the free energy of the system. As shown in Fig. 2, the location of a single particle is invariant with respect to position and direction in the planar LC film. The LC around the particle will re-orient and form a single half-Saturn ring defect. Two particles, however, introduce a new direction; as the free energy is minimized, the LC can get trapped in local minima that correspond to different directions with respect to the axis of the particles [72]. GL and MC relaxations were performed from a fixed LC initial orientation along the x -direction, $(1 \ 0 \ 0)$. Figure 3 shows the potential of mean force (PMF), $\psi = F - F_0$, as a function of the distance between particles, d , for different angles between the particles and the nematic field, α . The reference free energy, F_0 , is defined as the energy at the largest separation for each angle. For particles that are far apart, the PMF is independent of the orientation angle. As they get closer, the PMF becomes attractive ($\psi < 0$) or repulsive ($\psi > 0$), depending on the value of α .

Our results are summarized in Fig. 4, where the PMF is now plotted as a function of α for different particle separations. The figure reveals that, for orientations in the range $0^\circ < \alpha < 35^\circ$, the highest energy penalty occurs when particles are near each other. It is in this region where film and particles' directors differ the most, leading to the highest gradients and energy penalties. For

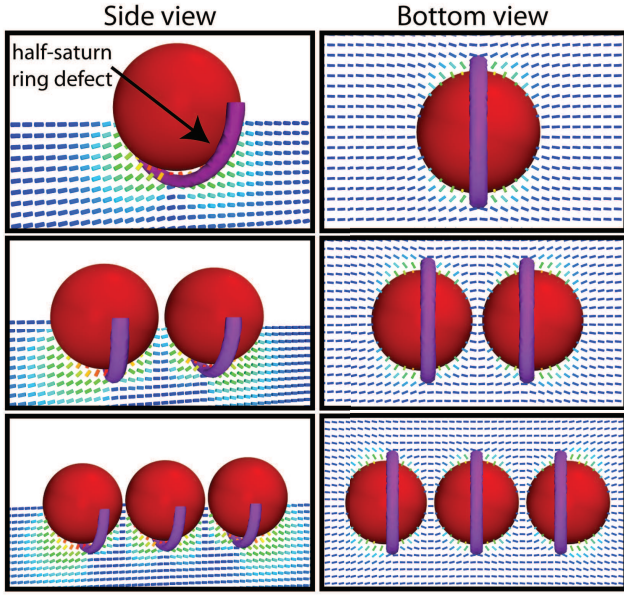


FIG. 2. Side and bottom views of particles ($r_p = 85$ nm) submerged in an LC degenerate planar film ($R = 500$ nm height). The strong homeotropic anchoring on the particles clashes with the director field of the film, leading to gradients that result in formation of a half-Saturn ring defect. Multiple particles are oriented in a manner that minimizes surface and elastic contributions to the free energy. The figure includes the final orientation field of the principal eigenvector \mathbf{n} and iso-surfaces of the scalar order parameter $S = 0.6$.

directors in the range $35^\circ < \alpha < 90^\circ$, the situation is reversed and the energy penalty reaches its minimum when particles are near each other. In this region, LC directors start to align along the particle's anchoring orientation, thereby decreasing the gradients. As a consequence, the defect configuration between the two particles leads to a lower energy penalty than having two independent defects. There are two angles that are worth highlighting: $\alpha = 35^\circ$ where the free energy is independent of particle separation (i.e. $\psi = 0$), and $\alpha = 75^\circ$, where the energy goes through a minimum for $d = 2\xi_N$. As the particle separation increases, the angle that set the energy minimum decreases (dotted line in Fig. 4): i.e. defects interact less as the distance between them increases.

Figures 5 and 6 summarize additional results for two and three particles from GL and MC free energy minimizations. Figure 6 presents the PMF as a function of the initial director orientation for different particle separations. As expected, the PMF follows the behavior of the two-particle system: the highest energy penalties are observed for $0^\circ < \alpha < 35^\circ$, while for $35^\circ < \alpha < 75^\circ$ we find the most favorable configurations. $\alpha = 75^\circ$ is also the most favorable configuration for adjacent particles, and the angle that corresponds to the energy minimum decreases as the particle separation increases.

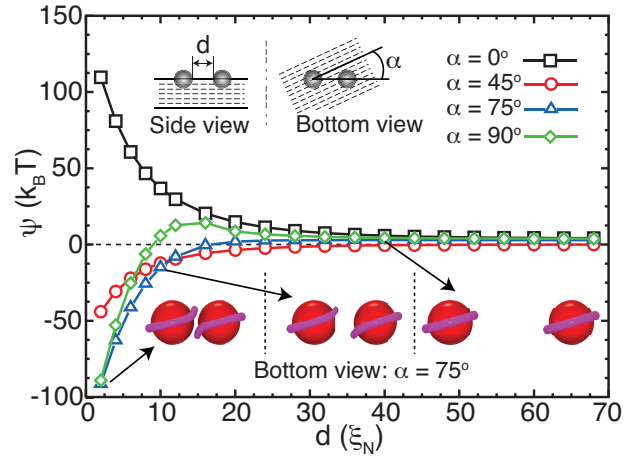


FIG. 3. Potential of mean force between two particles at an LC film, $\psi = F - F_0$, as a function of the distance between particles, d , for different angles between the particle separation axes and the nematic field, α . Final particle and defect arrangements, $S = 0.6$, for $\alpha = 75^\circ$ and three different separations.

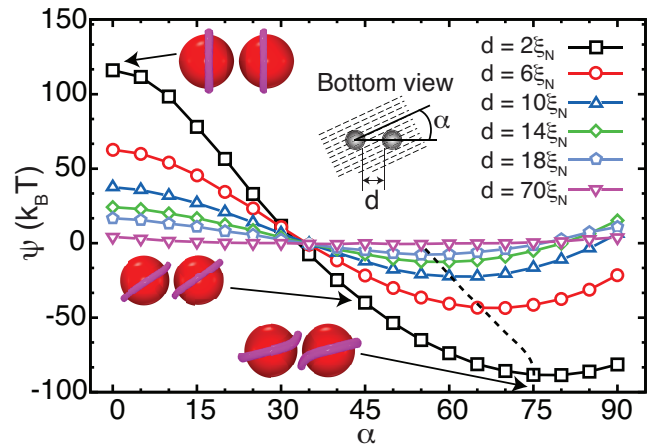


FIG. 4. Potential of mean force between two particles at an LC film, $\psi = F - F_0$, as a function of the relative angle between the LC and the particle separation axes for different particle separations, d . Final particle and defect arrangements, $S = 0.6$, for $d = 2\xi_N$. The location of the energy minimum follows the dotted line as the separation between particles increases.

B. LC droplet

For the LC droplet, sizes, anchoring strengths, temperature and number of particles were kept equal to those employed for the LC film. Unless otherwise stated, the GL and MC relaxations were started from a random director configuration.

For strong planar anchoring, the isolated LC droplet adopts a bipolar morphology (shown in Fig. 1) where two point defects, or boojums, are located at opposite poles.

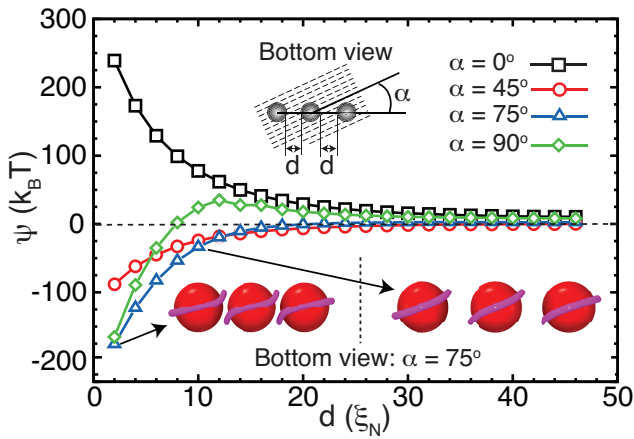


FIG. 5. Potential of mean force between three particles at an LC film, $\psi = F - F_0$, as a function of the distance between particles, d , for different angles between the particle separation axes and the nematic field, α . Final particle and defect arrangements, $S = 0.6$, for $\alpha = 75^\circ$ and two different separations.

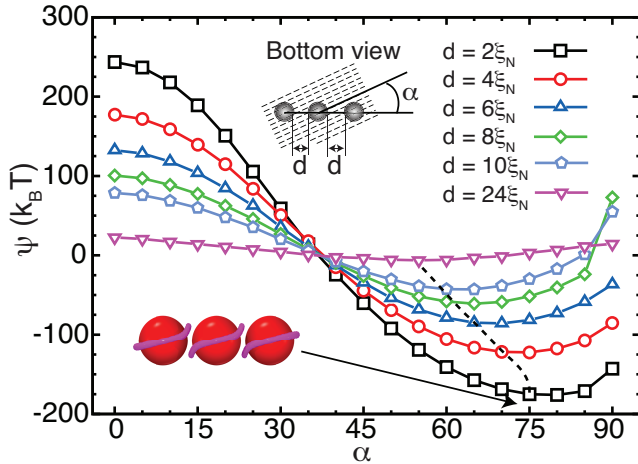


FIG. 6. Potential of mean force between three particles at an LC film, $\psi = F - F_0$, as a function of the relative angle between the LC and the particle separation axes for different particle separations, d . Final particle and defect arrangements, $S = 0.6$, for $d = 2\xi_N$. The location of the energy minima follows the dotted line as the separation between particles increases.

A clear difference between LC films and droplets is that, in droplets, half-submerged particles will perturb the LC orientation and will interact with the boojums. Figure 7 shows cross sections of representative configurations corresponding to one, two and three embedded particles. These were selected from an extensive portfolio of configurations and provide a representation of distortions, defects and phases. As shown in the closeups, the particles are driven to the boojums as an attempt to relax the surface/elastic distortions. Notice that when the particle is at the boojum, the half-saturn ring melts and disap-

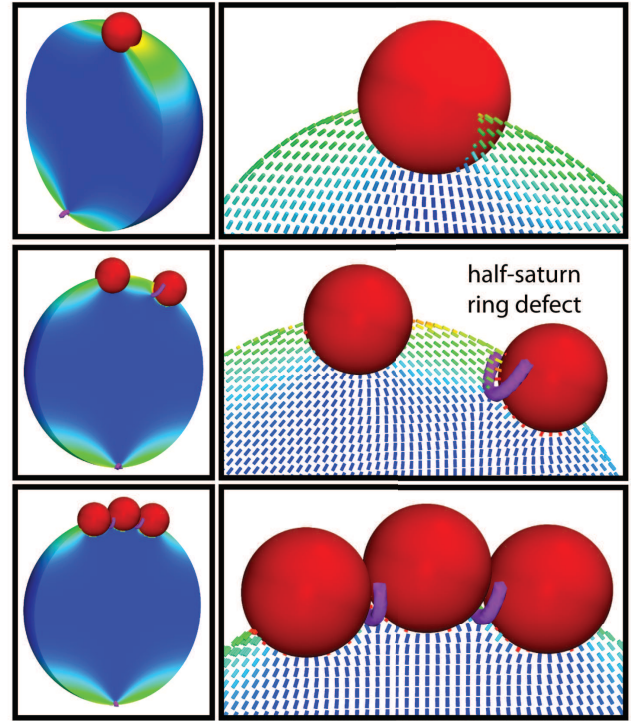


FIG. 7. Representative cross sections and closeups of particles ($r_p = 85$ nm) on the surface of an LC planar droplet ($R = 500$ nm). Color contours represent the relative direction between the local eigenvector \mathbf{n} and the averaged nematic direction: blue is for parallel and red is for perpendicular. Iso-surfaces of the scalar order parameter for $S = 0.6$ are shown in magenta.

pears.

For a single half-submerged particle, during energy minimization the LC changes its orientation in order to force one of the boojums to engulf the particle. These results agree with experimental observations [73–76] and calculations using molecular dynamics [10].

For two half-submerged particles, we fix one of them at the boojum and gradually change the position of the second (traveling) particle. The polar angle, θ_1 , is now defined as the angle between the axes connecting the droplet and the particles' centers. When $\theta_1 = 20^\circ$, the particles are almost touching, while $\theta = 180^\circ$ corresponds to particles located on opposite boojums. Figure 8 shows the free energy difference or PMF, $\psi = F - F_0$, as a function of the polar angle, where F_0 is the configuration with the lowest free energy. Final LC phases at the equilibrium state are also included in the figure. Intuitively, the lowest energy configuration is obtained when $\theta = 180^\circ$. This configuration leads to an energy minimum, since placing the particles at the existing boojums melts the half-Saturn ring around the particles. It is cheaper to melt the defects than to create extra defects by locating particles elsewhere. This arrangement is the closest to that of a pristine bipolar phase in an LC droplet with

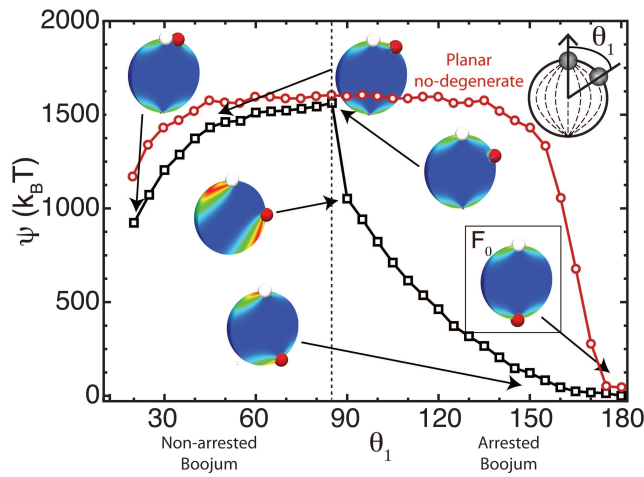


FIG. 8. Potential of mean force between two particles at an LC droplet, $\psi = F - F_0$ as a function of the particles' relative position, measured through the angle θ_1 . The black line corresponds to degenerate planar anchoring, while the red curve is for non-degenerate planar anchoring. Insets in the plot show the morphology at select particle separations, where the white particle is fixed at one boojum and the red particle is displaced by θ_1 .

no particles. When the particles are near each other, $\theta_1 = 20^\circ$, the droplet phase remains bipolar with both particles located at one boojum. This is a local minimum, with a free energy difference of $\sim 800 k_B T$. The additional energy cost corresponds to the small defect (not a complete half-Saturn ring) surrounding the particle that is not on the boojum.

As θ_1 increases from 20° , a series of interesting phenomena can be observed. The PMF increases continuously from $\sim 1000 k_B T$ to $\sim 1500 k_B T$. This difference corresponds to the creation of a full half-Saturn ring around the traveling particle. The PMF of $\sim 150 k_B T$ remains approximately constant until the angle reaches $\theta = 90^\circ$; note that in this range the droplet always exhibits two poles. At $\theta = 90^\circ$, there is a sudden decrease in the free energy because the free boojum is grabbed by the traveling particle. The system prefers to generate elastic distortions than having a full half-Saturn ring, i.e. now each particle possesses its own boojum. We divide this free energy diagram into: “non-arrested boojum” for $20^\circ < \theta_1 < 90^\circ$ and “arrested boojum” for $90^\circ < \theta_1 < 180^\circ$ (separated by the dotted line in Fig. 8). Previous calculations using molecular dynamics (MD) simulations of a many-body system [10] did not reveal arrested boojum configurations until $\theta_1 \sim 180^\circ$. Interestingly, when we adopt a model that enforces non-degenerate planar anchoring at the droplet (modeled through a Rapini-Paopular energy density), we recover the results of MD simulations for small droplets. The red line in Fig. 8 serves to emphasize that the restriction provided by non-degenerate anchoring eliminates the arrested boojum configurations, as it becomes more diffi-

cult for the system to generate elastic distortions.

It is well known that surface anchoring, W_F , and nematic strength, U (temperature or concentration), influence the equilibrium phase of LC droplets [77–79]. Figure 9 shows the energy densities, at the global minima, as a function of the surface anchoring for two temperatures: $U = 3$ and $U = 5$. Results are included for the Landau, elastic, surface and total energy differences for droplets without particles and with one and two particles. Note that weak anchoring results in uniform phases in the isolated droplet (no boojums); in that limit, the system prefers to enforce $\nabla \mathbf{n} = 0$, while for strong anchoring, it is preferable to have $\nabla \mathbf{n} \neq 0$ than to penalize surface anchoring. This transition is understood by following the monotonic increase in elastic energy as the anchoring is increased, as the surface energy reaches a maximum. At this maximum, it is preferable to undergo additional elastic distortions. Adding one or two particles decreases the anchoring strength at which this transition occurs. For strong anchoring, inclusion of particles always decreases the elastic and surface distortions. On the other hand, at low anchoring strengths, the particles penalize elastic distortions. As the temperature decreases (U increases), the energy differences increase and the transition anchoring strength moves towards weaker values, due to the increase in the nematic Landau free energy density.

For three half-submerged particles, the number of possible arrangements is considerably larger. In this work, we limit our analysis to three different sets of configurations: two iso-planar and one symmetric triangular arrangement.

The first iso-planar configuration fixes two particles at the boojums and moves a single particle. Figure 10 shows the PMF using the 2-1 configuration as the minimum reference energy (F_0). In this 2-1 configuration, at $\theta_1 = 10^\circ$, the particles are so close to each other that their defects merge, providing the lowest possible interaction between boojums and particles. As the polar angle, θ_1 , increases, the distance between particles also increases, providing enough room to form an individual half-Saturn ring defect around the traveling particle. The elastic penalty builds up until $\theta_1 \approx 40^\circ$. Inserts in Fig. 10 show the morphology for three different angles. Similar to the observations for two particles, the particles merge at the boojums.

Figure 11 summarizes the free energy difference as a function of the polar angle θ_2 . When the three particles are close to each other, almost touching, one boojum engulfs them, while the other remains at the opposite pole. As θ_2 increases, enough space is available for the formation of individual half-Saturn ring defects. Therefore, the free energy difference increases abruptly from $\sim 1000 k_B T$ to $\sim 5000 k_B T$. At this energy peak, where $\theta \sim 20^\circ$, the traveling particles trap the boojums, minimizing defects while maximizing elastic distortions (depicted red in the contours in Fig. 11). From this angle, the energy monotonically decreases. Notice that the $\theta_2 = 90^\circ$ is equivalent to the $\theta_1 = 90^\circ$ in Fig. 10. The $\theta_2 = 15^\circ$ ar-

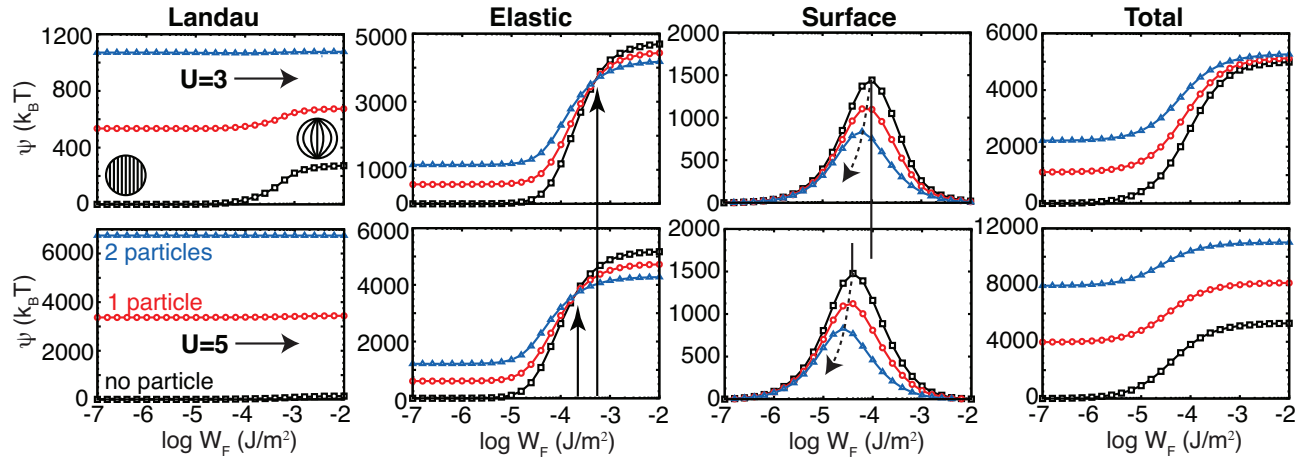


FIG. 9. Droplet free energy differences as a function of surface anchoring, for $U = 3$ (top) and $U = 5$ (bottom). A particle-free droplet is compared with one/two-particle droplets.

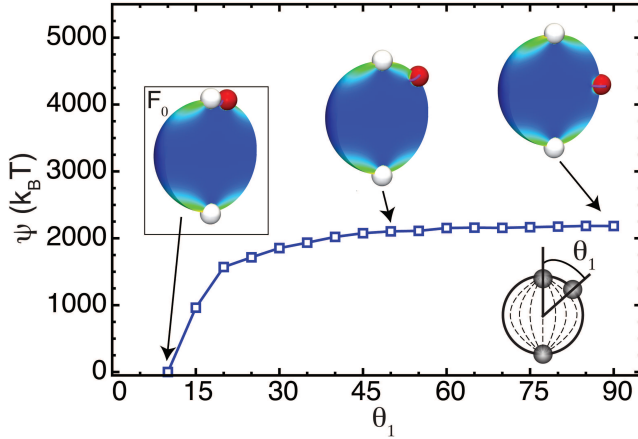


FIG. 10. Free energy difference as a function of the particles' arrangement for two particles (white) at the boojums and a single traveling (red) particle. The polar angle θ_1 measures particle separation. Inserts in the plot correspond to the minimum energy state for three representative values of θ_1 .

arrangement may be considered a local minimum, due to the high energy barrier that exists between this configuration and the 2-1, $\theta_1 = 10^\circ$ in Fig. 10. In other words, if during minimization the particles are nearby, the system will be trapped in the 3-0 configuration. Note that in the figure, red symbols (on top of black symbols) indicate that MC relaxations find the same final state that GL minimizations.

We finish this analysis by considering three particles arranged in a triangle on the droplet surface. Figure 12 summarizes the free energy differences as a function of polar angle θ_3 . For the closest arrangement, $\theta_3 = 10^\circ$, the particles form a consolidated defect and forces one boojum to the opposite pole (equivalent to $\theta_2 = 15^\circ$ in Fig. 11). When the distance between particles reaches a critical value, $\theta_3 \approx 25^\circ$, each particle develops its own

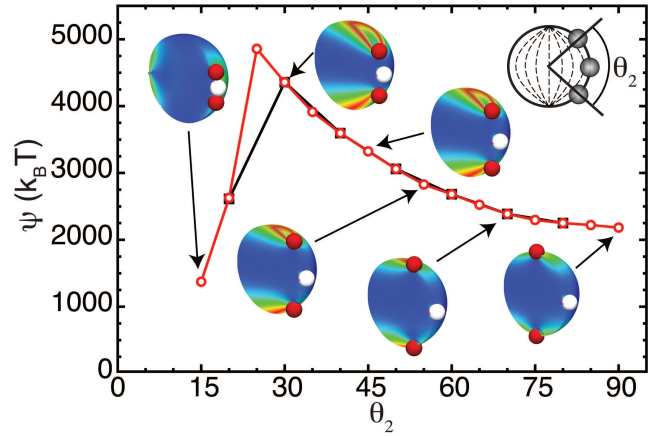


FIG. 11. Free energy difference as a function of the particles' arrangement for one fixed particle (white) and two traveling (red) particles. The polar angle θ_2 measures separation. Inserts in the plot correspond to the final phase at representative values of θ_2 .

defect, thereby incurring in the highest energy penalty. There are configurations where the free energy decreases: $\theta_3 = 25^\circ$ and $\theta_3 = 60^\circ$. These correspond to morphologies where one particle or two particles are near a boojum. These relaxations started from random configurations of the tensor order parameter.

V. CONCLUSIONS

In this work we considered the effects of nano-sized homeotropic particles adsorbed on nematic liquid crystalline surfaces. For concreteness, we focused on the case of strong anchoring, with nanoparticles of radius $r_p = 85$ nm, half-submerged in an LC droplet of $1 \mu\text{m}$ diameter. Past work with such systems has been limited

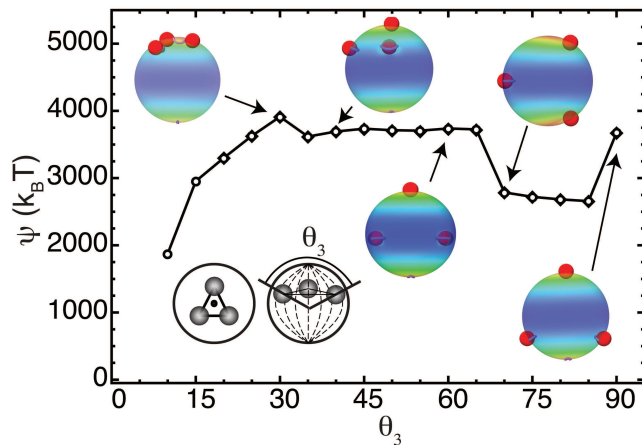


FIG. 12. Free energy difference as a function of the particles' arrangement in a triangular positioning. The polar angle θ_3 measures separation. Inserts in the plot correspond to the final phase at representative values of θ_3 .

to planar anchoring. These conditions are accessible in experiments with dark-field or fluorescence microscopy, and the predictions of our calculations could eventually be examined in experiments. When these particles are adsorbed on a flat interface, the particles exhibit an attraction energy of approximately $100 k_B T$ per particle. This attraction is induced by the underlying LC, and the relative particle orientation between the particle's separation axes and the director is 75° . Adding an additional third particle to the flat LC interface results in a larger free energy gain, but the particles' arrangement resembles that observed with two particles. When a particle is adsorbed at the interface of an LC bipolar droplet, it segregates to one of the boojums, thereby alleviating nematic distortions. The boojum and the particles' half-saturn ring merge with each other. The energy difference between having a free boojum and a boojum/particle is much larger, approximately $\sim 1000 k_B T$. In contrast to our observations for the flat interface, two particles in a bipolar LC droplet are localized in opposite boojums. The free energy difference between two particles sharing the same boojum or residing in opposite boojums is now $\sim 1000 k_B T$, an order of magnitude higher than observed on the flat interface. When a third particle is added, the formation of a half-saturn ring around that third particle increases the free energy by $\sim 2000 k_B T$. The additional particle therefore prefers to reside near one of the particles at one of the boojums. Because of the large penalty associated with a half-saturn ring, a large energy barrier must be overcome to move a particles from one boojum

to the other.

Past theoretical work with homeotropic nanoparticles in LC droplets was limited to many-body simulations of a Gay-Berne model and, as such, was limited to small nanoparticles and small droplets, with radii on scales of tens of nanometers. The results presented here were generated by relying on a continuum representation of the liquid crystal. They correspond to much larger systems and, as such, should facilitate comparison to future experiments. Note that, in general, the results of continuum calculations are consistent with those from many-body simulations, but the energy minima corresponding to particle localization or aggregation are much more pronounced. Specifically, Whitmer et al. [10] studied nanoparticles with weak homeotropic anchoring and a planar droplet; for the system sizes considered in that work the anchoring was uniform. The particle entrapment at the boojum reported here for degenerate anchoring occurs at lower angles than those observed by Whitmer et al.; when we consider non-degenerate anchoring in continuum simulations, however, our results converge onto those of Whitmer et al. More recently, Rahimi et al. [80] considered planar particles on a planar droplet. These authors found that the energy difference between two particles located on opposite boojums is approximately $700 k_B T$ lower than when they share a boojum (we obtain $1000 k_B T$ for homeotropic particles). For three particles, the global minimum also corresponds to two particles in one boojum and one particle in the other boojum; the main difference, however, is that for the planar case a third particle can be localized at a 90° angle with respect to the boojums, without formation of the half-saturn ring reported here, leading to the appearance of a local minimum.

ACKNOWLEDGMENTS

The authors acknowledge support from the Department of Energy, Basic Energy Sciences, Biomaterials Program under Grant No. DE-SC0004025. We acknowledge the University of Chicago Research Computing Center for use of the Midway cluster and support of this work. Argonne, a U.S. Department of Energy Office of Science laboratory, is operated under Contract No. DE-AC02-06CH11357. JCA-P is thankful to CONACYT for the Postdoctoral Fellowship Nos. 186166 and 203840. JPH-O is grateful to funding provided by the Universidad Nacional de Colombia Ph.D. grant and COLCIENCIAS under the Contract No. 110-165-843-748, "Patrimonio Autónomo Fondo Nacional de Financiamiento para la Ciencia, Tecnología y la Innovación Francisco José de Caldas."

[1] H. Mori, E. Gartland, J. Kelly, and P. Bos, *Jpn. J. Appl. Phys.* **38**, 135 (1999).

[2] J. M. Brake, M. K. Daschner, Y. Y. Luk, and N. L.

- Abbott, *Science* **302**, 2094 (2003).
- [3] J. K. Gupta, J. S. Zimmerman, J. J. de Pablo, F. Caruso, and N. L. Abbott, *Langmuir* **25**, 9016 (2009).
- [4] J. Zou and J. Fang, *Langmuir* **26**, 7025 (2009).
- [5] O. Lavrentovich, *Physica Scripta* **T39**, 394 (1991).
- [6] A. Sparavigna, L. Komitov, and A. Strigazzi, *Phys. Scripta* **42**, 210 (1991).
- [7] J. A. Moreno-Razo, E. J. Sambriski, N. L. Abbott, J. P. Hernandez-Ortiz, and J. J. de Pablo, *Nature* **485**, 86 (2012).
- [8] G. M. Koenig, I. H. Lin, and N. L. Abbott, *Proceedings Of The National Academy Of Sciences Of The United States Of America* **107**, 3998 (2010).
- [9] J. Moreno-Razo, E. Sambriski, G. Koenig, E. Díaz-Herrera, N. Abbott, and J. de Pablo, *Soft Matter* **7**, 6828 (2011).
- [10] J. Whitmer, X. Wang, F. Mondiot, D. Miller, N. Abbott, and J. de Pablo, *Phys. Rev. Lett.* **111**, 227801 (2013).
- [11] I.-H. Lin, D. S. Miller, P. J. Bertics, C. J. Murphy, J. J. D. Pablo, and N. Abbott, *Science* **332**, 1297 (2011).
- [12] H. Stark, *Physics Reports* **351**, 387 (2001).
- [13] O. Guzmán, E. B. Kim, S. Grollau, N. L. Abbott, and J. J. de Pablo, *Phys. Rev. Lett.* **91**, 235507 (2003).
- [14] F. R. Hung, B. T. Gettelfinger, G. M. K. Jr., N. L. Abbott, and J. J. de Pablo, *J. Chem. Phys.* **127**, 124702 (2007).
- [15] F. R. Hung, O. Guzmán, B. T. Gettelfinger, , N. L. Abbott, and J. J. de Pablo, *Phys. Rev. E* **74**, 011711 (2006).
- [16] M. Ravnik, M. Skarabot, S. Zumer, U. Tkalec, I. Poberaj, D. Babic, N. Osterman, and I. Musevic, *Phys. Rev. Lett.* **99**, 247801 (2007).
- [17] I. Musevic, M. Skarabot, U. Tkalec, M. Ravnik, and S. Zumer, *Science* **313**, 954 (2006).
- [18] J. Dontabhaktuni, M. Ravnik, and S. Zumer, *Soft Matter* **8**, 1657 (2012).
- [19] Z. Eskandari, N. M. Silvestre, and M. M. Telo da Gama, *Langmuir* **29**, 10360 (2013).
- [20] Z. Eskandari, N. M. Silvestre, M. M. Telo da Gama, and M. R. Ejtehadi, *Soft Matter* **10**, 9681 (2014).
- [21] F. Mondiot, X. Wang, J. J. de Pablo, and N. L. Abbott, *Journal Of The American Chemical Society* **135**, 9972 (2013).
- [22] J. C. Armas-Pérez, A. Londono-Hurtado, O. Guzmán, J. P. Hernández-Ortiz, and J. J. de Pablo, *J. Chem. Phys.* **Submitted** (2015).
- [23] M. Stephen and J. Straley, *Rev. Mod. Phys.* **46**, 617 (1974).
- [24] A. N. Beris and B. J. Edwards, *Thermodynamics of Flowing Systems* (Oxford University Press, Oxford, 1994).
- [25] T. C. Lubensky, *Phys Rev A-Gen Phys* **2**, 2497 (1970).
- [26] A. Saupe, *J. Chem. Phys.* **75**, 5118 (1981).
- [27] L. Longa and H.-R. Trebin, *Phys. Rev. A* **39**, 2160 (1989).
- [28] L. Longa, D. Monselesan, and H.-R. Trebin, *Liquid Crystals* **2**, 769 (1987).
- [29] T. J. Sluckin and A. Poniewierski, *Phys. Rev. Lett.* **55**, 2907 (1985).
- [30] P. Kaiser, W. Wiese, and S. Hess, *Journal of Non Equilibrium Thermodynamics* **17**, 153 (1992).
- [31] A. K. Bhattacharjee, G. I. Menon, and R. Adhikari, *Physical Review E* **78**, 026707 (2008).
- [32] A. K. Bhattacharjee, G. I. Menon, and R. Adhikari, *The Journal of Chemical Physics* **133**, 044112 (2010).
- [33] P. de Gennes and J. Prost, *The Physics of Liquid Crystals* (Oxford University Press, Oxford, 1995).
- [34] L. Landau and E. Lifshitz, *Statistical Physics*, 3rd ed. (Pergamon-Press, Oxford, 1980).
- [35] N. Kuzuu and M. Doi, *J. Phys. Soc. Japan* **52**, 3486 (1983).
- [36] O. Guzmán, N. Abbott, and J. de Pablo, *J. Poly. Sci. B* **43**, 1033 (2005).
- [37] O. Guzman, N. Abbott, and J. J. de Pablo, *J. Chem. Phys.* **122**, 184711 (2005).
- [38] S. Grollau, O. Guzman, N. Abbott, and J. J. de Pablo, *J. Chem. Phys.* **122**, 024703 (2005).
- [39] C. Oseen, *Trans. Faraday Soc.* **29**, 883 (1933).
- [40] C. Oseen, *Fortschr. Chem. Physik u. Physik. Chem.* **20**, 1 (1929).
- [41] C. Oseen, *Arkiv Matematik Astron. Fysik A* **19A**, 16 (1925).
- [42] Bernal, Lawrence, Oseen, H. Zocher, Kast, Ornstein, Feachem, N. K. Adam, Desch, Lowry, Rawlins, Hermmann, Foex, Malkin, Porter, Stewart, G. W. Stewart, A. M. Taylor, Ostwald, Carpenter, and G. S. Hartley, *Trans. Faraday Soc.* **29**, 1060 (1933).
- [43] F. Frank, *Discuss. Faraday Soc.* **25**, 19 (1958).
- [44] J. Ericksen, *Phys. Fluids* **9**, 1205 (1966).
- [45] E. C. Gartland and S. Mkaddem, *Phys. Rev. E* **59**, 563 (1999).
- [46] M. Papoular and A. Rapini, *Solid State Communications* **7**, 1639 (1969).
- [47] M. Nobili and G. Durand, *Phys Rev A* **46**, R6174 (1992).
- [48] M. Ravnik, G. P. Alexander, J. M. Yeomans, and S. Zumer, *Faraday Discuss.* **144**, 159 (2010).
- [49] M. Skarabot, M. Ravnik, S. Zumer, U. Tkalec, I. Poberaj, D. Babic, N. Osterman, and I. Musevic, *Phys. Rev. E* **76**, 051406 (2007).
- [50] F. R. Hung, *Phys. Rev. E* **79**, 021705 (2009).
- [51] J. Fournier and P. Galatola, *Europhys Lett* **72**, 403 (2005).
- [52] O. D. Lavrentovich, *Liquid Crystals* **24**, 117 (1998).
- [53] T. Porenta, M. Ravnik, and S. Zumer, *Soft Matter* **7**, 132 (2011).
- [54] O. O. Prishchepa, A. V. Shabanov, and V. Y. Zyryanov, *Phys. Rev. E* **72**, 031712 (2005).
- [55] O. Prishchepa, A. Shabanov, and V. Zyryanov, *JETP. Lett.* **79**, 257 (2004).
- [56] A. Golemme, S. Zumer, J. Doane, and M. Neubert, *Phys. Rev. A* **37**, 559 (1988).
- [57] E. Dubois-Violet and O. Parody, *J. de Physique Colloques* **30**, C4 (1969).
- [58] S. I. Hernández, J. A. Moreno-Razo, A. Ramírez-Hernández, E. Díaz-Herrera, J. P. Hernández-Ortiz, and J. J. de Pablo, *Soft Matter* **8**, 1443 (2011).
- [59] Q. Ji, R. Lefort, R. Busselez, and D. Morineau, *J Chem Phys* **130**, 234501 (2009).
- [60] R. Berardi, A. Costantini, L. Muccioli, S. Orlandi, and C. Zannoni, *J Chem Phys* **126**, 044905 (2007).
- [61] R. K. Goyal and M. M. Denn, *Phys. Rev. E* **75**, 021704 (2007).
- [62] W. M. Brown, M. K. Petersen, S. J. Plimpton, and G. S. Grest, *J. Chem. Phys.* **130**, 044901 (2009).
- [63] G. S. Preeti, N. Satyavathi, K. P. N. Murthy, and V. S. S. Sastry, *Liquid Crystals* **36**, 1379 (2009).
- [64] C. Chiccoli, P. Pasini, and F. Semeria, *Mol. Cryst. Liq. Cryst.* **221**, 19 (1992).
- [65] T. Gruhn and S. Hess, *Zeit. Naturforsch. A* **51**, 693 (1996).
- [66] R. W. Ruhwandl and E. M. Terentjev, *Phys. Rev. E* **56**,

- 5561 (1997).
- [67] E. Kreyszig, *Advanced Engineering Mathematics*, 8th ed. (John Wiley & Sons, New York, 1999).
- [68] B. T. Gettelfinger, J. A. Moreno-Razo, G. M. K. Jr., J. P. Hernández-Ortiz, N. L. Abbott, and J. J. de Pablo, *Soft-Matter* **6**(5), 896 (2010).
- [69] J. P. Hernandez-Ortiz, B. T. Gettelfinger, J. Moreno-Razo, and J. J. D. Pablo, *J Chem Phys* **134**, 134905 (2011).
- [70] S. Chandrasekhar, *Liquid Crystals*, 2nd ed. (Cambridge University Press, Cambridge, 1992).
- [71] O. Guzman and J. J. de Pablo, *J. Chem. Phys.* **118**, 2392 (2003).
- [72] V. Tomar, T. F. Roberts, N. L. Abbott, J. P. Hernandez-Ortiz, and J. J. de Pablo, *Langmuir* **28**, 6124 (2012).
- [73] F. Mondiot, X. Wang, J. J. de Pablo, and N. L. Abbott, *Journal of the American Chemical Society* **135**, 9972 (2013).
- [74] X. Wang, D. S. Miller, J. J. de Pablo, and N. L. Abbott, *Advanced Functional Materials* **24**, 6219 (2014).
- [75] P. Mushenheim, R. Trivedi, D. Weibel, and N. Abbott, *Biophysical Journal* **107**, 255 (2014).
- [76] D. S. Miller, X. Wang, and N. L. Abbott, *Chemistry of Materials* **26**, 496 (2014).
- [77] V. Tomar, S. I. Hernandez, N. L. Abbott, J. P. Hernandez-Ortiz, and J. J. de Pablo, *Soft Matter* **8**, 8679 (2012).
- [78] G. Volovik and O. Lavrentovich, *Zh. Eksp. Teor. Fiz.* **85**, 1997 (1983).
- [79] A. Golemme, S. Zumer, D. Allender, and J. Doane, *Phys. Rev. Lett.* **61**, 2937 (1988).
- [80] M. Rahimi, T. F. Roberts, J. C. Armas-Pérez, X. Wang, E. Bukusoglu, N. L. Abbott, and J. J. de Pablo, *Proceedings Of The National Academy Of Sciences Of The United States Of America* (2015).

